OPEN ACCESS
IOP Publishing

Superconductor Science and Technology

Supercond. Sci. Technol. **37** (2024) 125002 (11pp)

https://doi.org/10.1088/1361-6668/ad8122

Effect of thermal annealing on the average and local structure of superconducting polycrystalline NbRe films

Z Makhdoumi Kakhaki[1], A Martinelli[2], F Avitabile[3], A Di Bernardo[1], C Attanasio[1] and C Cirillo[3,*]

[1] Dipartimento di Fisica 'E.R. Caianiello', Università degli Studi di Salerno, I-84084 Fisciano (Sa), Italy
[2] CNR-SPIN, Corso Perrone 24, 16152 Genova, Italy
[3] CNR-SPIN, c/o Università degli Studi di Salerno, I-84084 Fisciano (Sa), Italy

E-mail: carla.cirillo@spin.cnr.it

Received 20 December 2023, revised 3 September 2024
Accepted for publication 27 September 2024
Published 24 October 2024

Abstract

Nb_xRe_{1-x} is a non-centrosymmetric superconductor recently realized in thin film form. The access to the basic physics that governs this material is hindered by the polycrystalline structure of the films which consist of grains of small dimensions. In these conditions, films are not decisive in revealing the nature of the superconducting order parameter, and, in particular, the possible presence of a spin-triplet component. In this work, post-deposition annealing procedures were performed to improve the crystalline quality of the as-grown films. As determined by x-ray diffraction measurements, by tuning the annealing process, it was possible to increase the crystalline size from 1–2 nm up to several nanometers, beyond the values of the superconducting coherence length. Pair distribution function analyses revealed the non-centrosymmetric crystal structure of the treated NbRe films. Finally, electrical transport measurements, performed to study the relationship between structural and transport properties of the samples, showed an improved metallicity and a reduction of the superconducting critical temperature after the thermal treatment. This last result can be reasonably ascribed, for instance, to oxygen contamination, modification of the electronic density of states at the Fermi level, or change in the electron–phonon coupling. The results of this work are useful to realize films for future experiments meant to access nature of the superconducting order parameter.

Keywords: thin films, superconductivity, pair-distribution function analysis, x-ray diffraction, thermal annealing

* Author to whom any correspondence should be addressed.

1. Introduction

The renewed interest in non-centrosymmetric superconductors (NCS) lies in the possible intrinsic presence of spin-triplet superconducting correlations, namely unconventional Cooper pairs with equally aligned spins, in these systems [1, 2]. This is intimately connected to the crystal structure of NCS, which lacks of inversion symmetry with respect to specific lattice positions. A strong spin–orbit scattering is also a crucial ingredient to observe mixed singlet–triplet pairing state. Therefore, the class of NCS transition-metal compounds containing heavy elements is deeply investigated. These materials may in principle host a two-components order parameter, consisting of pairs of electrons with both antiparallel (singlet) and parallel (triplet) spin alignment. In particular, systems containing Rhenium atoms showed interesting, but often controversial behavior [3–6] and, recently, it was suggested that Re itself may enclose an admixed singlet-triplet pairing [7]. Among Re-based NCS, Nb_xRe_{1-x} (hereafter NbRe) is one of the most studied materials. In order to access to the pairing symmetry of the superconducting order parameter, it is desirable to have NbRe in single-crystal form. Single-crystals, available only in the case of bulk samples [8], showed the presence of two gaps by directional soft point contact measurements [9], but they were not conclusive about the possible presence of a triplet component. Recently, we succeeded in growing textured polycrystalline NbRe films by UHV magnetron sputtering technique [10]. Conventional x-ray diffraction (XRD) studies on polycrystalline NbRe films revealed the presence of a single broad peak [10, 11] corresponding to the 330 reflections of the α-Mn cubic phase [12, 13]. By using the Scherrer approach, the dimensions of the nanocrystallites were estimated of about 2–3 nm [11]. However, this technique cannot provide detailed information about the disordered structure of these films, which we believe is responsible for the conductance spectra typical of a single-gap s-wave superconductor measured in tunnel junctions based on them [10]. We expect that this discrepancy between the results (single gap in films and two gaps in single crystals) can be overcome by improving the crystalline quality of the films. In a previous paper, by varying the deposition conditions, we analysed the relationship between crystallographic and superconducting transport properties of as-grown films [11]. Preliminary investigations suggest that post-deposition thermal treatments at temperatures $\approx$600 °C produce films with higher texture [11]. However, a systematic study of the effect of the annealing on the structural and superconducting properties of NbRe films is still lacking. In general, one may expect that post-deposition annealing, by increasing mobility of atoms, promotes grain growth and coalescence [14]. Different parameters, such as annealing temperature, T_{ann}, and time, as well as heating and cooling rates play a role in these processes. Thermal annealing is often applied also to superconducting thin films to select a specific crystallographic phase [15], to improve the superconducting properties [16, 17], or to study the more fundamental problem of the interplay between superconductivity and disorder [18]. In this last respect, reduced grain dimensions can also affect the values of T_c as a result of a modification of the electronic density of states at the Fermi level [19, 20] and of the strength of the electron-phonon coupling [21]. In this work, we tuned the post-deposition annealing of NbRe films by systematically varying the process parameters with the final goal of obtaining films with larger crystallite size and improved crystallographic orientation, which can be suitable to perform reliable pairing-sensitive measurements. The structural properties of the resulting films, with different thickness and grown on different substrates, were investigated by XRD. Synchrotron x-ray pair distribution function (PDF) analysis [22] was also performed on thick films (d_{NbRe} = 150 nm). PDF is particularly suitable in amorphous or nanocrystalline systems in which a short-range ordering is present (such as NbRe), and can access to the local atomic structure of the materials. This technique, never applied on NbRe, can be useful to deepen the knowledge of the crystallographic properties of this material in thin film form and, in particular, to verify the non-centrosymmetric nature of the unit cell. In addition, electrical transport measurements were performed to evaluate the superconducting critical temperature, T_c, and the normal state properties, such as the residual resistivity ratio (RRR) of the annealed films.

2. Experimental details

NbRe films were deposited by dc magnetron sputtering in a ultra-high vacuum system with a base pressure in the low 10^{-8} mbar range from a stoichiometric $Nb_{0.18}Re_{0.82}$ target. This composition was preserved in the films, as evaluated by energy dispersive spectroscopy (EDS) measurements. The films were grown on different substrates, mainly p-doped (100)-oriented silicon (Si), 300 nm-thick silicon oxide (SiO_2), and occasionally R-plane sapphire (Al_2O_3). Films were sputtered at $W = 250$–300 Watt in a Ar pressure $P_{Ar} = 4$ μbar at room temperature, with a resulting rate of about 0.2 nm s^{-1}. Films of different thicknesses (d_{NbRe} = 20–150 nm) were deposited. We analyzed both the as-grown films and those subjected to thermal annealing processes. For clarity, films in the low (high) thickness limit were named by the letter L (H) followed by a number indicating d_{NbRe} in nm, and a sequentially numbered suffix. The annealing processes were performed in a Carbolite Gero tube furnace under Ar atmosphere. The effect of annealing temperature and the ramp rate were investigated. For comparison, some films in the intermediate thickness range were annealed in vacuum. A Bruker D2 Phaser x-ray diffractometer in a specular Bragg-Brentano geometry was used to structurally characterize the films by XRD measurements. The values of the lattice parameter, a, and of the crystallites size, t, were evaluated from high angle θ-2θ pattern by using a source of CuK_α ($\lambda = 1.541\,84$ Å) and CuK_β ($\lambda = 1.392\,22$ Å) radiation at 30 kV and 10 mA. Synchrotron x-ray elastic scattering data were collected at room temperature at the ID11 beamline of the European Synchrotron Radiation Facility (ESRF- Grenoble, France) using a wavelength $\lambda = 0.1809$ Å and a Dectris Eiger4M CdTe detector. A 1x1 mm edge size fragment was selected from each thin film and mounted a sample stage with movement in x, y, z, as well as θ and ω rotations. Data collection was carried out using a grazing-incidence geometry. Reduction of the total scattering for obtaining the $G(r)$ function (the reduced PDF function) was achieved using PDFgetX3 software [23] with $Q_{\max} = 22.4$ Å. Full-profile fitting of the $G(r)$ function was carried out using the PDFgui software [24]. In the structural model, the occupations of the cationic sites were fixed to the nominal compositions provided by Scanning Electron Microscopy-EDS analysis. In the last cycle of the fitting, the following parameters were refined: the scale factor, the unit-cell parameters, the anisotropic atomic displacement parameters, the dynamic correlation factor, and the parameter related to the finite size of the diffracting domain (spdiameter). Finally, the parameters describing the experimental resolution effects (Q_{damp} and Q_{broad}) were fixed to the values refined using a standard CeO_2 sample. Electric transport measurements were performed in a ^{4}He cryostat using a standard dc four-probe technique on unpatterned samples biased with a dc current of $I_b = 0.5$ mA.

3. Results

In this section, we report the annealing procedures which we developed to optimize the crystallinity of our NbRe films. We varied parameters such as annealing temperature, time, heating and cooling rates, as well as treatment steps. As it will be clear in the following, these processes also affect the superconducting properties. In particular, the growth of the grains always produces a decrease of T_c. Therefore, our efforts were focused on finding a balance between enhancing crystallinity and preserving high-T_c values. For clarity, we decided to present the data according to the thickness of the analyzed films. First, we discuss the optimization of thinner films with $d_{\text{NbRe}} = 20$ and 30 nm. This thickness range is particularly sensitive to changes in superconducting properties and is often employed in proximity effect related experiment [25]. Then we describe the annealing recipes developed for the thick films, for which we benefited from the results obtained in the regime of low d_{NbRe}. On these films pair distribution analysis was also performed to study the effect of the annealing on the local structure of the films.

3.1. Thin films

Our study started with the optimization of the annealing procedures of films with $d_{\text{NbRe}} = 20$ and 30 nm. A summary of the main characteristics of the films annealed according to different recipes is reported in table 1.

Typical broad peaks, indexed as 330 reflections, of the as-grown films named L30-1 and L20-1 are reported in figures 1(a) and (b) with open symbols, respectively. This peak is the only peak present in the XRD profile, apart from the 400 reflection corresponding to the substrate (not shown) [11]. From the analysis of the XRD profile the lattice parameter (a) and the dimensions of the grains in the growth direction (t) were evaluated by using the Bragg law ($a = (\lambda\sqrt{h^2+k^2+l^2})/2\sin\theta$, here $h = k = 3$ and $l = 0$ are the Miller indexes) and Scherrer equation ($t = 0.9\lambda/B\cos\theta$), respectively. In the previous formulas, θ is the diffraction angle and B is the full width at half maximum of the diffraction peak [26]. For both films values comparable to the ones previously reported are obtained with $a \approx 9.4$ Å and $t \approx 2$ nm [11]. Similar result was also obtained for the as-grown film 20 nm-thick deposited on SiO_2, L20-2 (not shown in figure 1(b)). After deposition, the films were thermally treated in an inert flowing Ar atmosphere. The first goal was to determine the optimal temperature of the process, while fixing the heating and cooling rate at 250–300 °C h^{-1} and the time of treatment at 1 h, as already tested in [11]. We annealed the films at $T_{\text{ann}} = 400$ °C, 500 °C, 600 °C and 700 °C (see films L30-2, L30-3, L30-4, and L30-7 in table 1). It resulted that for $T_{\text{ann}} = 400$ °C (sample L30-2) and 500 °C (sample L30-3) both the position and the width of the 330 peak are almost identical to those measured in the pre-annealing state. On the other hand, as shown in figure 1(a) by the green line (sample L30-4), after the annealing at $T_{\text{ann}} = 600$ °C, the width of the 330 reflection (the only one present after the treatment) is reduced. This result is accompanied by an enhancement of the intensity. This correspond to a remarkable increase in the grain size ($t = 11$ nm). However, the superconducting properties of the film were suppressed, and no transition was recorded above $T = 4.2$ K. Both these results are in accordance with those of [11]. Conversely, increasing the duration to a total of two hours at the same T_{ann} (sample L30-6) or T_{ann} up to 700 °C (sample L30-7) produced a decrease of both a and t. Therefore, we fixed $T_{\text{ann}} = 600$ °C and we reduced the time of the treatment to 30 min. Sample L30-5 results from this annealing procedure. Its 330 reflection (shown in figure 1(a) by the purple line) gives $t = 8$ nm, which is lower than that of sample L30-4. However, it exhibits a larger critical temperature, $T_c = 5.12$ K. It is evident that the annealing procedure needs to be carefully tuned to achieve a balance between increasing the grain size and suppressing the critical temperature. This kind of systematic study was performed on the samples of series L20-x with $d_{\text{NbRe}} = 20$ nm (see table 1). On these films we investigated the effect of the substrate (Si and SiO_2), the annealing time (which never exceeded 30 min), the annealing rate (300 and 600 °C h^{-1}), and annealing profile on both structural and superconducting properties. These results are summarized in figure 1, where the diffraction peaks (figure 1(b)) and the normalized resistive transitions (figure 1(c)) for representative films from the series L20-x are reported. First, we used the same recipe (600 °C (30 min) at 300 °C h^{-1}) applied to obtain sample L30-5 on films grown on both substrates. This procedure produced a relevant increase of the grain size, as it can be inferred from the XRD measurements (figure 1(b)) by comparing the result of the as-grown film on Si (L20-1) to those of samples L20-3 ($t = 7.8$ nm) and L20-4 ($t = 6.6$ nm), grown respectively on Si and SiO_2. Also in this case the values of T_c are significantly depressed for both samples compared to the as-grown films (see figure 1(c) and table 1).

Then we acted on another parameter, namely the heating rate and we performed the annealing procedure at $T_{\text{ann}} =$

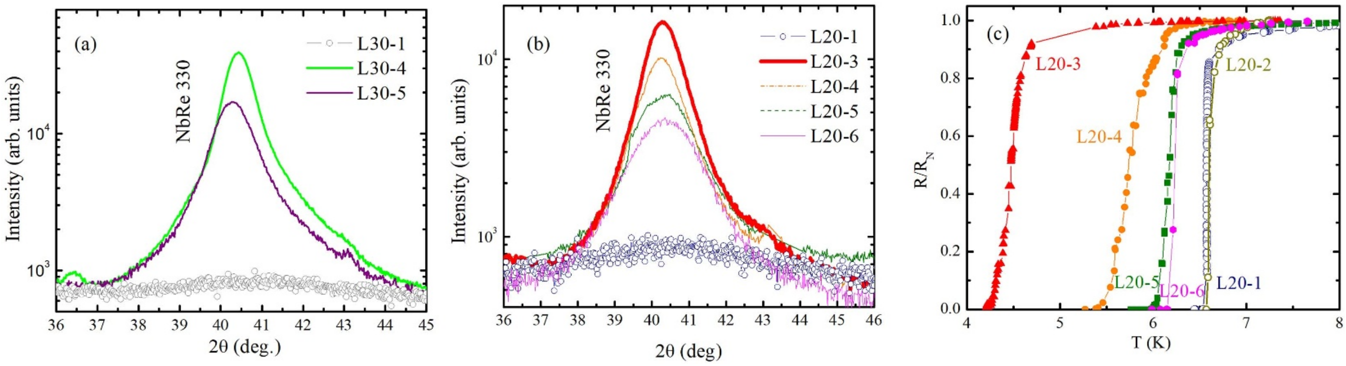

Figure 1. Comparison of diffraction peaks corresponding to the 330 reflection for the films: (a) L30-1, L30-4, and L30-5, (b) L20-1, L20-3, L20-4, L20-5, and L20-6. (c) Normalized $R(T)$ transitions for the set of films L20-1 to L20-6.

Table 1. Name, substrate, thickness, structural parameters, and superconducting properties of the films with $d_{\mathrm{NbRe}} = 20$ and 30 nm under study.

Sample name	Substrate	Annealing recipe	d_{NbRe} (nm)	T_c (K)	ΔT_c (K)	RRR	t (nm)	a (Å)
L30-1	Si	as grown	30	6.14	0.17	0.947	1.6	9.43
L30-2	Si	400 °C (1 h) at 300 °C h^{-1}	30	insulating	—	—	1.6	9.43
L30-3	Si	500 °C (1 h) at 300 °C h^{-1}	30	insulating	—	—	1.6	9.43
L30-4	Si	600 °C (1 h) at 300 °C h^{-1}	30	<4.2	—	1.13	11	9.47
L30-5	Si	600 °C (30 min) at 300 °C h^{-1}	30	5.12	0.16	1.02	8	9.49
L30-6	Si	600 °C (2 h) at 300 °C h^{-1}	30	insulating	—	—	—	—
L30-7	Si	700 °C (1 h) at 300 °C h^{-1}	30	insulating	—	—	—	—
L20-1	Si	as grown	20	6.60	0.13	0.63	1.7	9.43
L20-2	SiO_2	as grown	20	6.60	0.13	0.61	1.7	9.37
L20-3	Si	600 °C (30 min) at 300 °C h^{-1}	20	4.48	0.33	1.12	7.8	9.49
L20-4	SiO_2	600 °C (30 min) at 300 °C h^{-1}	20	5.73	0.53	1.04	6.6	9.50
L20-5	Si	600 °C (30 min) at 600 °C h^{-1}	20	6.17	0.19	0.98	4.8	9.50
L20-6	SiO_2	600 °C (5 min) at 600 °C h^{-1}	20	6.24	0.17	1.00	4.4	9.46
L20-7	Al_2O_3	600 °C (5 min) at 600 °C h^{-1}	20	5.93	0.27	1.06	—	—
L20-8	SiO_2	600 °C (30 min) + 300 °C (30 min) at 600 °C h^{-1}	20	6.28	0.14	1.05	7.4	9.49
L20-9	SiO_2	600 °C (30 min) + 300 °C (1 h) at 600 °C h^{-1}	20	6.05	0.23	1.02	5.6	9.48
L20-10	SiO_2	as grown	20	5.47	0.07	—	—	—
L20-11	SiO_2	under vacuum 600 °C (30 min) + 300 °C (30 min) at 600 °C h^{-1}	20	6.85	0.10	—	2.4	9.45

600 °C at the rate of 600 °C h^{-1}. The resulting film (L20-5) has $T_c = 6.17$ K, much closer to that of L20-1 (figure 1(c)). However, this procedure resulted to be less effective in increasing the grain size, which resulted to be only 4.8 nm (figure 1(b) and table 1). The increased heating speed leads to a higher number of nucleation centers, resulting in more grains with similar and intermediate dimensions, instead of fewer, larger grains which are thermodynamically more stable [27].

We then decided to further tune the annealing time, reducing it down to 5 min. This recipe was tested on films grown on both SiO_2 (L20-6) and Al_2O_3 (L20-7) substrates. From figure 1(c) we notice that L20-6 has a small T_c shift of about 0.36 K compared to the corresponding as-grown film. However, the increase in t (estimated to be 4.4 nm from the peak in figure 1(b)) is smaller than that observed for film L20-5, which was annealed for 30 min. On the contrary, sample L20-7 after the annealing has a much lower T_c. Moreover, the position of the substrate peak is almost superimposed to the 330 reflection (not shown), and this affects the correct determination of t and a. For both these reasons, we decided to restrict our study to Si and SiO_2.

Figure 2 summarizes the effect of the annealing time and of the ramp rate (both 300 and 600 °C h^{-1}) on the crystallographic (panel (a)) and superconducting (panel (b)) properties. It emerges that a significant increase of t and a requires an annealing time of at least 30 min. It is also evident that a faster heating/cooling procedure preserves the T_c values and improves the metallicity, but does not optimize the grain size. At this stage, we added a second step in the annealing protocol, namely, we kept the films at an intermediate temperature of $T'_{\mathrm{ann}} = 300$ °C before the complete cool down to room temperature. The purpose was to extend the thermal treatment for longer time, while reducing the possible source of interdiffusion from the substrate and contamination from the furnace environment. These factors could, in principle, be responsible for the depression of T_c. Therefore, additional annealings

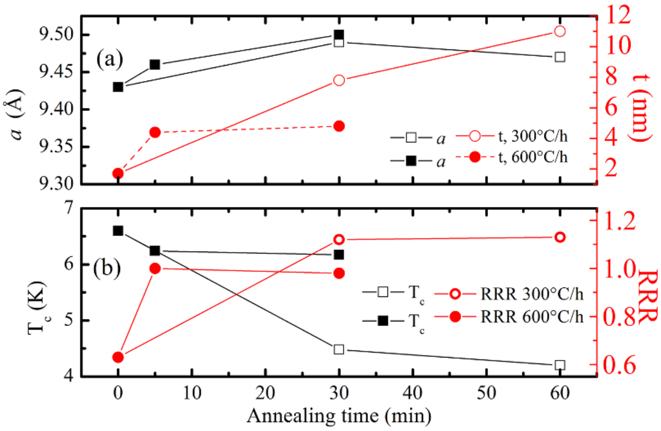

Figure 2. Effect of the annealing time and heating rate at 600 °C on (a) the crystalline properties (lattice parameter (left scale) and grain size (right scale)) and (b) electrical characteristics (T_c (left scale) and RRR (right scale)).

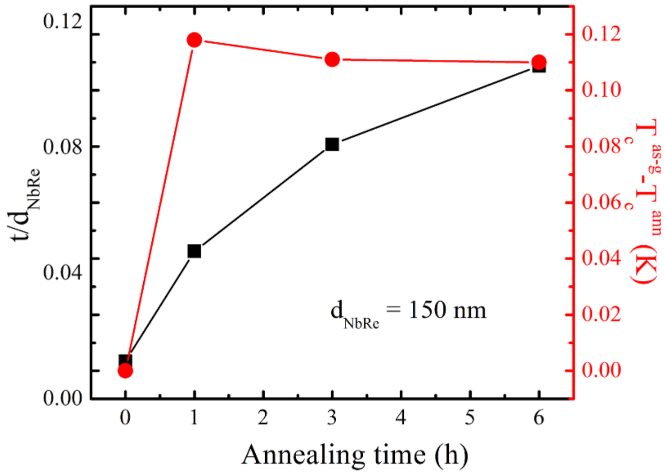

Figure 4. Effect of the annealing time at 600 °C on the ratio between the grain size and the film thickness (left scale) and T_c depression (right scale).

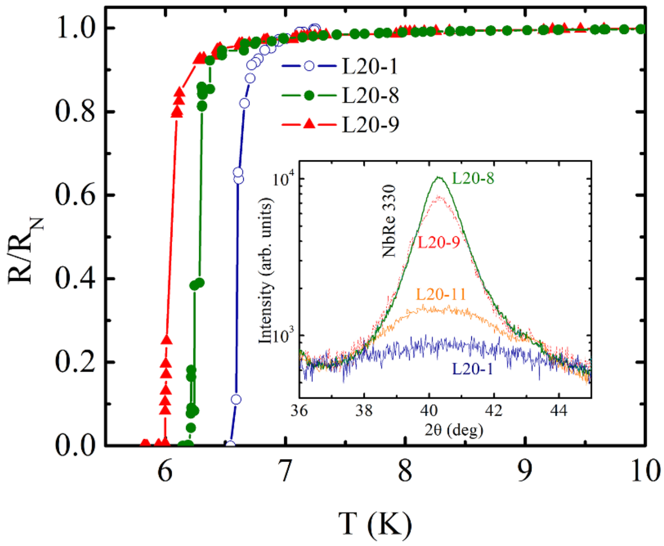

Figure 3. Normalized resistive transitions for the as-grown film named L20-1 compared to the films annealed at 600 °C (30 min) with a rate of 600 $°C\,h^{-1}$ on SiO_2 and subjected to the additional heating at $T'_{ann} = 300$ °C for 30 min (L20-8) and 1 h (L20-9). Inset: XRD patterns for the films L20-8 and L20-9, compared to the ones of the as-grown film (L20-1) and the film annealed under vacuum (L20-10).

of 30 min (L20-8) and 1 h (L20-9) were tested. The resulting $R(T)$ and XRD patterns are compared to the same measurements performed on the as-grown film L20-1 in figure 3. Interestingly, this recipe leads to both larger grains and higher critical temperature with respect to the film L20-5, treated according to the same rate and time, but without the second annealing step (see table 1). To summarize, the best compromise between grain growth and T_c suppression is obtained with an additional annealing at $T'_{ann} = 300$ °C for 30 min. The resulting sample (L20-8) has, indeed, $t = 7.4$ nm and $T_c = 6.28$ K.

Finally, the annealing procedure according to these optimized conditions (600 °C (30 min) + 300 °C (30 min) at 600 $°C\,h^{-1}$) was also performed under vacuum in order to reduce the possible presence of residual gases, such as oxygen, acting as contaminants during the thermal process. A base pressure of 2×10^{-5} mbar was achieved by pumping the furnace by turbomolecular pump. The annealing procedure was then performed by keeping the furnace pumped. The XRD profile obtained on this sample (L20-11) is shown in the inset of figure 3 by orange line. The pattern is better defined compared to that of a typical as-grown film of the same thickness (L20-1, blue line), as it reflects an increased grain size of $t = 2.4$ nm. However, the crystallite dimensions are about one third of the ones obtained for sample L20-8, annealed in the same conditions but in Ar flux (see table 1). This indicates that the presence of the inert Ar gas promotes an easier growth of the grains. Moreover, it may improve thermal coupling and increase the conductivity. Interestingly, for the film L20-11 an increase of T_c of about 0.4 K compared to the as grown film (L20-10) was registered (see table 1). This result supports the idea that oxygen contamination may be responsible of the critical temperature reduction. We will address this issue in more detail in the discussion.

3.2. Thick films

Having tuned the main annealing procedures in the thin-film limit, we extended our study to thick films ($d_{NbRe} = 150$ nm) on which PDF analysis was also performed. Taking advantage of the previous results, we kept fixed the annealing temperature at 600 °C and the ramp rate at 600 $°C\,h^{-1}$, and we preliminary analysed the role of the annealing time.

Indeed, annealing for the established time of 1 h was not sufficient to obtain a relevant value for the t/d_{NbRe} ratio. Structural and electrical characterization of a preliminary set of thick films annealed for 1 h up to 24 h at 600 °C (30 min) at 600 $°C\,h^{-1}$, evidence that, to preserve superconductivity and maximize grain size, an annealing time of 6 h is optimal. This is summarized in figure 4, which shows the effect of the annealing time at 600 °C on the grain size (left scale) and on

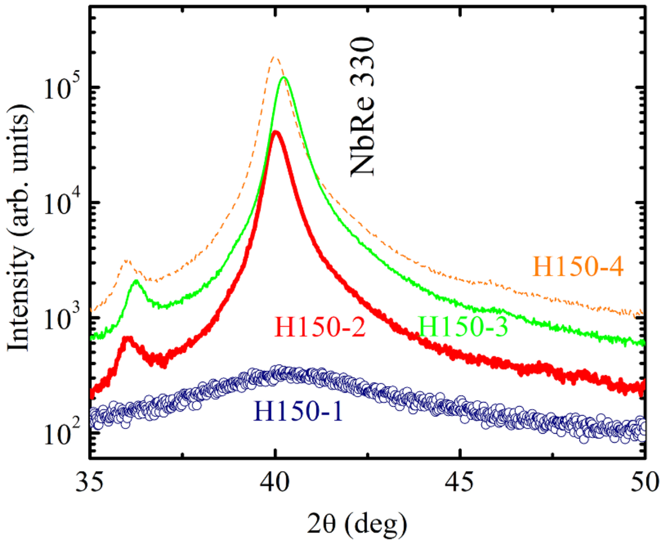

Figure 5. Diffraction peaks corresponding to the 330 reflection for the films H150-1–H150-4.

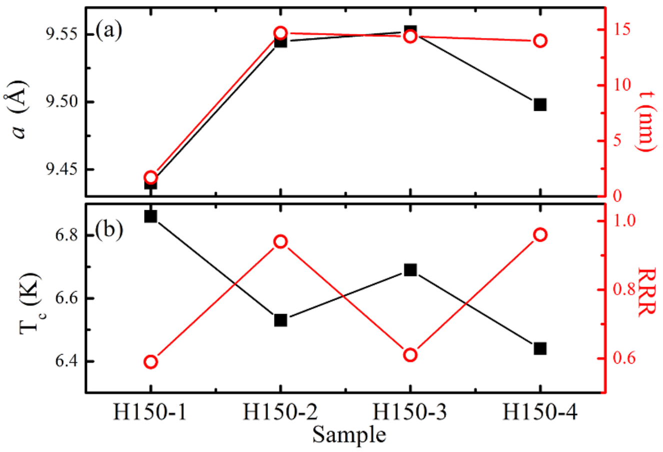

Figure 6. (a) Lattice parameter (left axis) and mean grain size (right axis) for the 150 nm films deposited on different substrates and annealed under different conditions as summarized in table 2. (b) Superconducting critical temperature (left scale) and residual resistivity ratio (right scale) for the same samples.

Table 2. Name, substrate, thickness, structural parameters, and superconducting properties of the films with $d_{\mathrm{NbRe}} = 150$ nm under study.

Sample name	Substrate	Annealing recipe	d_{NbRe} (nm)	T_c (K)	ΔT_c (K)	RRR	$\rho_{10\,\mathrm{K}}$ ($\mu\Omega$·cm)	t (nm)	a (Å)
H150-1	Si	as grown	150	6.86	0.02	0.59	300	1.7	9.44
H150-2	Si	600 °C (6 h) at 600 °C h^{-1}	150	6.53	0.11	0.94	181	14.7	9.54
H150-3	SiO_2	600 °C (6 h) at 600 °C h^{-1}	150	6.69	0.10	0.61	—	14.4	9.55
H150-4	Si	600 °C (6 h) + 300 °C (1 h) at 600 °C h^{-1}	150	6.44	0.05	0.96	196	14.0	9.50

the depression of the critical temperature (defined as the difference between the T_c of the as-grown film ($T_c^{\mathrm{as-g}}$) and the T_c of the annealed one (T_c^{ann})) (right scale). The point corresponding to a treatment of 24 h is not reported since no XRD peaks were observed in the diffraction pattern and the sample was also insulating. For this reason, all the films analyzed in the following were annealed for 6 h. A summary of the main characteristics of these investigated films, on which the PDF analysis was also performed, is reported in table 2. In the following, the effect of both the substrate choice (Si for films H150-1, H150-2, H150-4 and SiO_2 for film H150-3) and of the plateau at 300 °C for 1 h (H150-4) was analyzed.

The 330 reflection of an as-grown film (H150-1) is compared to the annealed ones in figure 5. All the annealed films present peaks with higher intensities and lower widths. The thermal treatment produced an increase in the grain size, from 1.7 nm (sample H150-1) up to about 14 nm for all the analysed films (see table 2). This result is reported on the right scale of figure 6(a). The left scale of the same panel refers to the values of the lattice constant, which, despite the clear increase, is still lower with respect to the one estimated for single crystals ($a = 9.6507$ Å) [12]. As results from figure 6(a), in this thickness regime, good crystalline properties were obtained independently on the substrate and the addition of the plateau at 300 °C. The effect of the thermal treatment on the transport properties also reveals interesting results. On one hand, these optimized annealing parameters do not significanlty alter the values of T_c (figure 6(b), left axis). This result is reasonable if we suppose that interdiffusion from the substrate or increased roughness may come at play during the heating process. The consequences of both these effects are expected to be less important for thick films. On the other hand, there is a correlation between the T_c depression, increased metallicity (namely increased RRR) (figure 6(b), right axis) and improved texture. Indeed, samples H150-2 and H150-4, with increased grain size, have not only low values of T_c, but also RRR close to unity (see figure 6(b), right axis) and lower values of low temperature resistivity (ρ_{10K}), compared to the as-grown film (see table 2). Therefore, these results may support the scenario of an intrinsic effect, as already reported in other materials [19, 20].

On these samples (H150-1–H150-4) synchrotron x-ray elastic scattering measurements were performed. Topological constraints are expected to hold to some extent even in materials characterized by low degree of crystallinity, thus implying that structural properties of crystalline phases can be recognised also in poorly crystallized samples, at least on the local scale. PDF yields structural information at the local scale from amorphous, nanostructured and crystalline materials. In particular, the position of the PDF peaks is given by the values of the bond lengths in the inspected sample, whereas their width depends on the bond distance fluctuations (depending on thermal vibrations and static atomic disorder). Figure 7 shows the high resolution (HR) XRD normalized data obtained at the ID11 beamline. The profiles evidence the different structural properties of the sample H150-1 compared to the annealed ones. Indeed, the diffraction pattern of the sample H150-1 exhibits a completely different profile, and it is also characterized by a much higher background, clearly indicating a higher structural disorder. Fainter differences mark the remaining patterns. In particular, the broadened peak at about 1.5 $Å^{-1}$ observed for sample H150-1 is still present in patterns corresponding to the films H150-2 and H150-4. This broad peak is absent for the sample H150-3 (the only one grown on SiO_2), which, on the contrary, shows two faint peaks at about 1.05 $Å^{-1}$ and 2.00 $Å^{-1}$, hardly observed also in the H150-2 sample.

Figure 8(a) shows the experimental $G(r)$ functions, representing the probability to find two atoms separated by a distance r (thus corresponding to a histogram of interatomic distances), for all the inspected films. Samples H150-2, H150-3 and H150-4 are characterized by a first and strong peak at about 2.71 Å exhibiting a shoulder at around 3.2 Å. These bond distances are in fair agreement with those measured in the χ-phase of the NbRe system, crystallizing in the I$\bar{4}$3 m space

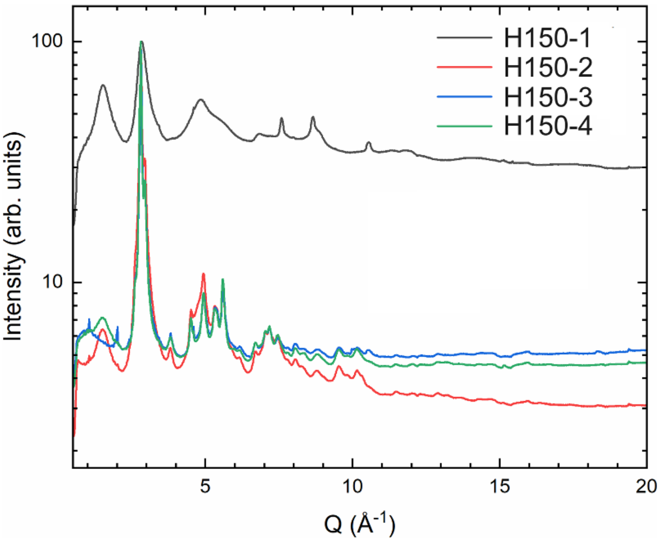

Figure 7. Synchrotron XRD data obtained for the films H150-1—H150-4. For a better comparison among the samples, the data are normalized and plotted in logarithmic scale.

group. Conversely, H150-1 shows two distinct peaks at about 2.4 Å and 2.9 Å in the same distance region. Such a feature indicates that sample H150-1 is characterized by significantly different structural properties, even at the local scale.

Since the peak width yields information about static and/or dynamic disorder of the atoms involved in the pair, it is interesting to observe the evolution of the peak width for different samples. It is evident that the H150-2 sample is significantly more ordered than the films H150-3 and H150-4. This conclusion agrees with the fact that this sample also exhibits a lower background. In particular, it is useful to compare samples H150-2 and H150-4 grown on Si, which were prepared by applying the same thermal treatment, but with and additional annealing at lower temperature in the case of H150-4. Despite this, both HR-XRD and PDF data indicate that the amount of structural disorder is larger for sample H150-4. It is not clear the reason for this behaviour. Likely, the formation of domains or other non-diffusive phenomena are activated during the treatment at low temperature, detrimental for the overall crystallinity. It is important to notice that the experimental *G(r)* functions obtained for all the annealed films can be successfully fitted using a cubic I$\bar{4}$3 m structural model. Figure 8(b) shows the fitting for the H150-2 sample, selected as representative. It is evident that the fit gets worst below ≈9 Å, whereas for longer distances the structural model fits reasonably well the experimental data. This result indicates that significant structural distortions affect the material at the local scale.

The same cubic I$\bar{4}$3 m structural model was applied to fit the HR-XRD data by applying the Rietveld method, but it was rejected due to the low quality of the result. This outcome indicates that this structural model can be quite reasonably used as a reference at the local scale, but its reliability vanishes as the distance increases. Nonetheless, the peak at about 2.9 $Å^{-1}$ observed in all the HR-XRD patterns (figure 7) can

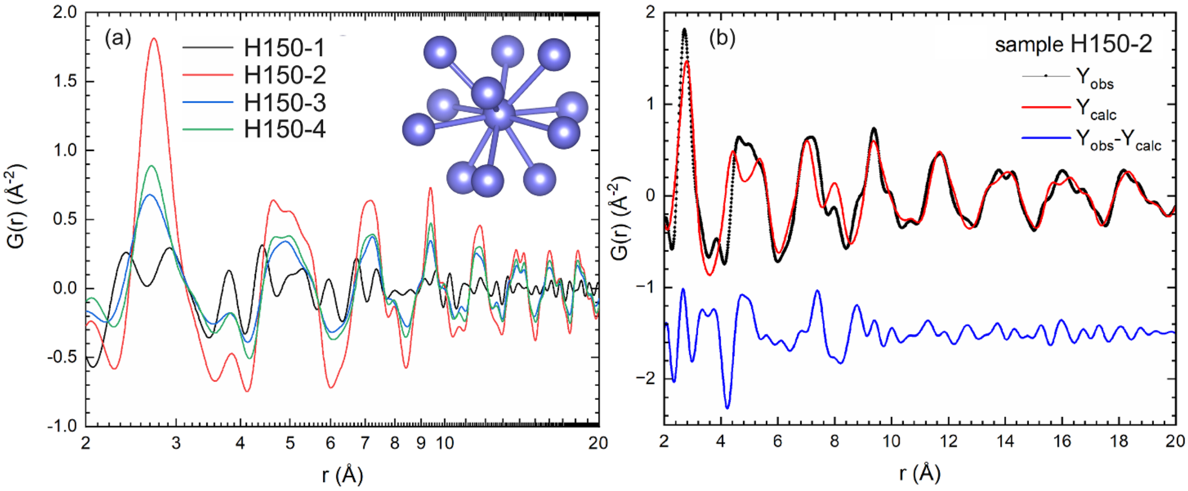

Figure 8. (a) Experimental $G(r)$ functions obtained for the different NbRe films. Data are plotted on a logarithmic scale in order to highlight data at shorter r values. The inset shows the bond distances corresponding to the first shell about 2.4 Å and 3.1 Å. (b) Experimental G(r) functions obtained for the H150-2 sample fitted with a I$\bar{4}$3 m structural model.

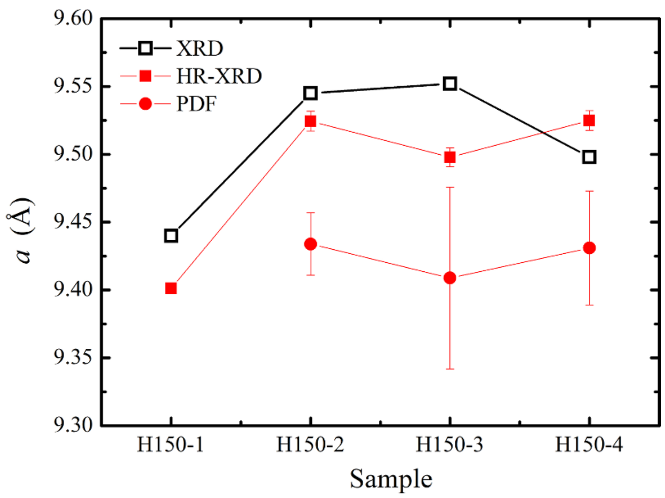

Figure 9. Comparison of the cell parameter for the analysed samples as obtained by different techniques.

be indexed as 330 in the cubic I$\bar{4}$3 m structural model. Given the cubic symmetry, it is possible to determine acceptable cell parameter values by fitting this single diffraction peak.

Figure 9 shows the comparison of the cell parameters as obtained by fitting the $G(r)$ functions and the 330 diffraction line in the HR-XRD patterns. A quite fair agreement is observed between the two data sets, their differences being related to the different distance scale probed by HR-XRD (red closed squares) and PDF (red closed circles). Moreover, it is also evident that the as-grown film (H150-1) is characterized by a significantly lower value of a compared to the annealed films independently on substrate and thermal treatment. It is interesting to observe that the cell parameter mainly depends on the substrate rather than on thermal treatments, at least for this optimized annealing recipes, since samples H150-2 and H150-4 were both deposited on Si and underwent different thermal treatments, whereas N3 was deposited on SiO_2. Finally, it is worth commenting about the good agreement between the values of a obtained from the standard XRD (black open squares) and the HR-XRD measurements, which also emerges from figure 9. The same happens for the estimation of t. Generally speaking, the experimental $G(r)$ function can provide a direct estimation of the coherent diffracting domains average size. In fact, as the structural coherence is progressively suppressed with distance, a damping of the $G(r)$ function data is observed. By the fall-off in amplitude of the $G(r)$ peaks, the range of the structural coherence for the as-grown sample can be estimated about 5 nm, whereas for the annealed films it is ≈15 nm. These numbers are in reasonable agreement with those extracted from the analysis of the standard XRD patterns by using the Scherrer formula.

4. Discussion

We have explored several recipes to enhance the crystal quality of NbRe films of different thickness. In the regime of $d_{\mathrm{NbRe}} =$ 20–30 nm, by an appropriate thermal treatment we were able to increase the dimensions of the crystal grains from about 1–2 up to 11 nm, without significantly affecting the superconducting properties. This corresponds to a value of t/d_{NbRe} of about 0.4 for the film L30-4. The annealed films with $d_{\mathrm{NbRe}} = 150$ nm have crystallites' size of about 14-15 nm and clearly show the expected I$\bar{4}$3 m non-centrosymmetric crystal structure. In this sense, it seems irrelevant the reduction of T_{c} produced by the annealing in Ar flow. This depression is less pronounced for the thick films and, moreover, the $R(T)$ curves are relatively narrow for all the films. For example, the width of the superconducting transitions, defined as $\Delta T_{\mathrm{c}} = T_{\mathrm{c}}^{90\%} - T_{\mathrm{c}}^{10\%}$, for all the films of the series L20-x never exceeds 0.53 K. Different mechanisms can be responsible for the T_{c} suppression, such for instance, a change in the film composition [12], a possible oxygen contamination, or an intrinsic effect directly related a modification of the electron–phonon coupling [21] or electron density of states at the Fermi level [19, 20]. In the following we analyze all these possible scenarios. First, we performed EDS measurements to compare the chemical composition of the films annealed by different recipes with the as grown ones. It resulted that, for all the investigated samples, the Nb and Re atomic concentration ratio is Nb/Re $\approx$ 14/86 both for annealed and as grown films. On the other hand, interdiffusion from the substrates or oxidation reactions due to oxygen residues in the furnace can explain why the T_{c} suppression is less pronounced in the case of thick films and for short annealing time. The results obtained on films annealed in vacuum further support the possibility of samples' poisoning during the process in Ar. In this case, the process is less efficient in terms of grains' growth, but a small increase in T_{c} is obtained. The latter can be also due to oxygen degassing from the films, with a consequent reduction of the microstrain induced by the interstitial oxygen atoms. As far as the possible intrinsic correlation between the dimensions of the grains and T_{c}, it is worth to notice that this result is consistent with that reported for NbRe films in [11]. Also in that case, by changing the deposition conditions, small improvements in the dimensions of the grains was accompanied by a small depression of T_{c}. This result is not surprising, since when the characteristic dimensions of a superconductor are comparable to the superconducting coherence length, ξ, it can show behaviors that, due to nanostructuring or small grain dimensions, are significantly different from the bulk. This is because dimensional effects are important for both electron–phonon interaction and for the electronic density of states [21]. T_{c}, in particular, depends on both effects. The combination and the balance between the two contributions determine if the critical temperature is enhanced or depressed as a function of the dimensional reductions. The dimensional effects have different consequences depending on the material characteristics and, in particular, on the ratio l/ξ_0 (here l is the electronic mean free path and ξ_0 is the superconducting coherence length in the clean limit). Very specific measurements and simulations must be performed at this purpose, which are beyond the scope of this work.

The evident result of this work is that it produced a relevant change in the crystallite size with significant effects both on the superconducting and normal state properties. Indeed, the transition from the regime $t < \xi(0)$ to $t > \xi(0)$ is observed, where $\xi(0) = 4.8$ nm [10]. Moreover, the larger values of RRR observed for the annealed films indicate an improved metallicity of the films, and hence, reasonably, an increase of l, reported of about 5 nm in the case of polycrystalline samples [12]. Therefore, a proper annealing unequivocally reduces the contribution of grain boundary scattering and enables reliable pairing sensitive experiments. Here, we want to stress that, even if the single crystal condition, $t = d_{\mathrm{NbRe}}$, was not fulfilled, this work represent a non-trivial extension of the research field on NCS. To date, NbRe is the only NCS available in thin film form. Here, PDF analyses performed on the data collected at ESRF demonstrated that films annealed according to the optimized protocol show the correct non-centrosymmetric crystal structure. The availability of these samples may help in shading a light in the debate on the symmetry of the superconducting order parameter in this system. Indeed, the main goal of our research was to provide samples on which pairing sensitive experiments, such as Scanning Tunnelling Microscopy (STM) could be performed. STM proved to be a powerful technique which gives direct access to the superconducting order parameter, as widely demonstrated in high temperature [28], multiple-gap [29], or recently in spin-triplet [30] superconductors. Indeed, STM can provide important information concerning the number and the symmetry of the order parameters, as reported for instance for non-centrosymmetric Ru_7B_3 [31]. However, tunnel measurements require directionality in the current injection with respect to the crystallographic axes. In the present work we succeed in obtaining oriented NbRe films with grains of dimensions larger than the superconducting coherence length and with the expected non-centrosymmetric structure. On these optimized films it will be possible to perform reliable direction-controlled experiments by STM. Moreover, new Squid-on-tip platforms [32] may be used to locally map critical temperature or critical fields. Finally, the crystallographic properties of the films may be further improved by growing the film on substrates heated at the temperature used in our optimized annealing protocol.

5. Conclusions

Films of NbRe in different thickness regimes were deposited on different substrates and subjected to various thermal treatments. The as-grown films have a polycrystalline structure with small crystallites and transport properties typical of disordered films (RRR < 1). A clear improvement in the dimensions of the grains and lattice parameter was obtained by tuning the annealing procedures. In particular, in the low thickness regime ($d_{\mathrm{NbRe}} = 20$–30 nm) the ratio between the grain size and the thickness can reach about $t/d_{\mathrm{NbRe}} \approx 0.4$. The PDF analysis was performed on the thick films by assuming they have a $I\bar{4}3$ m structure. Despite the limits imposed by the experimental set-up, the fit of the experimental data, is satisfactory. Moreover, the different XRD techniques return the same trend in the increase of the grain and lattice constant, despite the small difference in the estimated values of t and a. For all the investigated films, the increase in the crystallite size corresponds to a small depression of T_c, as already reported in [11]. This study shades a light on the experiments performed so far on as-grown NbRe films [10, 25] and on the discrepancy with the results obtained on single crystals [9]. In this respect, this work opens new perspectives in terms of possible experiments to be performed on annealed films. Should the spin-triplet component being proven to be the dominant pairing mechanism, it may open new perspectives for realizing devices that exploit spin-polarized supercurrents (superconducting spintronics) [33]. Finally, the access to the local structure of the NbRe films obtained by PDF is of fundamental importance. Indeed, the microscopic knowledge of the material allows a correct theoretical modelling of the system necessary to interpret the experimental results obtained on the NbRe films where still many questions are open.

Data availability statement

The data cannot be made publicly available upon publication because they are not available in a format that is sufficiently accessible or reusable by other researchers. The data that support the findings of this study are available upon reasonable request from the authors.

Acknowledgments

This work was carried out with the support of the European Synchrotron Radiation Facility, (Proposal MA-5616; DOI: 10.15151/ESRF-ES-1117383187). A M acknowledges E Bright for her kind assistance during data collection. This work is part of the Project IR0000003—IRIS supported by the NextGeneration EU-funded Italian National Recovery and Resilience Plan with the Decree of the Ministry of University and Research Number 124 (21/06/2022) for the Mission 4—Component 2—Investment 3.1.

ORCID iDs

A Martinelli https://orcid.org/0000-0001-8391-3486
F Avitabile https://orcid.org/0009-0009-3926-9609
C Attanasio https://orcid.org/0000-0002-3848-9169
C Cirillo https://orcid.org/0000-0001-8755-4484

References

[1] Bauer E and Sigrist M 2012 *Non-Centrosymmetric Superconductors: Introduction and Overview* (Springer)

[2] Smidman M, Salamon M B, Yuan H Q and Agterberg D F 2017 Superconductivity and spin–orbit coupling in non-centrosymmetric materials: a review *Rep. Prog. Phys.* **80** 036501

[3] Singh R P, Hillier A D, Mazidian B, Quintanilla J, Annett J F, Paul D M, Balakrishnan G and Lees M R 2014 Detection of time-reversal symmetry breaking in the noncentrosymmetric superconductor Re_6Zr using muon-spin spectroscopy *Phys. Rev. Lett.* **112** 107002

[4] Singh D, Barker J A T, Thamizhavel A, Paul D, Hillier A D and Singh R P 2017 Time-reversal symmetry breaking in the noncentrosymmetric superconductor Re_6Hf: further evidence for unconventional behavior in the α-Mn family of materials *Phys. Rev.* B **96** 180501(R)

[5] Shang T *et al* 2018 Nodeless superconductivity and time-reversal symmetry breaking in the noncentrosymmetric superconductor $Re_{24}Ti_5$ *Phys. Rev.* B **97** 020502(R)

[6] Shang T *et al* 2018 Time-reversal symmetry breaking in Re-based superconductors *Phys. Rev. Lett.* **121** 257002

[7] Csire G, Annett J F, Quintanilla J and Ujfalussy B 2022 Magnetically textured superconductivity in elemental rhenium *Phys. Rev.* B **106** L020501

[8] Singh R P, Smidman M, Lees M R, McK Paul D and Balakrishnan G 2012 Crystal growth of the non-centrosymmetric superconductor $Nb_{0.18}Re_{0.82}$ *J. Cryst. Growth* **361** 129

[9] Cirillo C, Fittipaldi R, Smidman M, Carapella G, Attanasio C, Vecchione A, Singh R P, Lees M R, Balakrishnan G and Cuoco M 2015 *Phys. Rev.* B **91** 134508

[10] Cirillo C, Carapella G, Salvato M, Arpaia R, Caputo M and Attanasio C 2016 Superconducting properties of noncentrosymmetric $Nb_{0.18}Re_{0.82}$ thin films probed by transport and tunneling experiments *Phys. Rev.* B **94** 104512

[11] Cirillo C, Caputo M, Divitini G, Robinson J W A and Attanasio C 2022 Polycrystalline NbRe superconducting films deposited by direct current magnetron sputtering *Thin Solid Films* **758** 139450

[12] Chen J, Jiao L, Zhang J L, Chen Y, Yang L, Nicklas M, Steglich F and Yuan H Q 2013 BCS like superconductivity in the noncentrosymmetric compounds Nb_xRe_{1-x} ($0.13 < x < 0.38$) *Phys. Rev.* B **88** 144510

[13] Periyasamy M, Bradshaw H, Sukenik N, Alpern H, Yochelis S, Robinson J W A, Millo O and Paltiel Y 2020 universal proximity effects in hybrid superconductor–linker molecule–nanoparticle systems: the effect of molecular chirality *Appl. Phys. Lett.* **117** 242601

[14] Ohring M 1992 *Materials Science of Thin Films* (Elsevier)

[15] Kalal S, Tayal A, Karmakar S, Joshi R, Rawat R and Gupta M 2023 Electron–phonon interactions and superconductivity of β-Nb_2N thin films *Appl. Phys. Lett.* **122** 072602

[16] Guziewicza M *et al* 2011 Technology of ultrathin NbN and NbTiN films for superconducting photodetectors *Acta Phys. Pol.* A **120** A-76

[17] Farrahi T and Eller M B 2019 Effect of deposition annealing on the structural and electrical properties of NbTiN thin films deposited by reactive bias target ion beam deposition technique *IEEE Trans. Appl. Supercond.* **29** 1103205

[18] Crauste O, Gentils A, Couedo F, Dolgorouky Y, Berge L, Collin S, Marrache-Kikuchi C A and Dumoulin L 2013 Effect of annealing on the superconducting properties of a-Nb_xSi_{1-x} thin films *Phys. Rev.* B **87** 144514

[19] Sides W D, Hassani E, Pappas D P, Hu Y, Oh T-S and Huang Q 2020 Grain growth and superconductivity of rhenium electrodeposited from water-in-salt electrolytes *J. Appl. Phys.* **127** 085301

[20] Haberkorn N, Bengio S, Suarez S, Perez P D, Hofer J A and Sirena M 2019 Effect of thermal annealing and irradiation damage on the superconducting critical temperature of nanocrystalline γ-Mo_2N thin films *Mater. Lett.* **236** 252

[21] Lozano D P *et al* 2019 Experimental observation of electron-phonon coupling enhancement in Sn nanowires caused by phonon confinement effects *Phys. Rev.* B **99** 064512
[22] Billinge S J L 2019 The rise of the x-ray atomic pair distribution function method: a series of fortunate events *Phil. Trans. R. Soc.* A **377** 20180413
[23] Juhás P, Davis T, Farrow C L and Billinge S J L 2013 A rapid and highly automatable program for processing powder diffraction data into total scattering pair distribution functions *J. Appl. Cryst.* **46** 560
[24] Farrow C L, Juhás P, Liu J W, Bryndin D, Bozvin E S, Bloch J, Proffen T and Billinge S J L 2007 Computer programs for studying nanostructure in crystals *J. Phys.: Condens. Matter* **19** 335219
[25] Cirillo C, Rovirola M, González C, Casals B, Hernàndez J M, Macià F, García-Santiago A and Attanasio C 2023 Spin pumping in NbRe/Co superconductor-ferromagnet heterostructures *Supercond. Sci. Technol.* **36** 074001
[26] Cullity B D 1978 *Elements of X-ray Diffraction* (Addison-Wesley Publishing Company Inc.)
[27] Thompson C V 1990 Grain growth in thin films *Annu. Rev. Mater. Sci.* **20** 245
[28] Fischer Ø, Kugler M, Maggio-Aprile I, Berthod C and Renner C 2007 Scanning tunneling spectroscopy of high-temperature superconductors *Rev. Mod. Phys.* **79** 353
[29] Giubileo F, Roditchev D, Sacks W, Lamy R, Thanh D X, Klein J, Miraglia S, Fruchart D, Marcus J and Monod P 2001 Two-gap state density in MgB_2: a true bulk property or a proximity effect? *Phys. Rev. Lett.* **87** 177008
[30] Gu Q *et al* 2023 Detection of a pair density wave state in UTe_2 *Nature* **618** 921
[31] Datta S *et al* 2021 Spectroscopic evidence of mixed angular momentum symmetry in non-centrosymmetric Ru_7B_3 *Sci. Rep.* **11** 21030
[32] Blom T J, Mechielsen T W, Fermin R, Hesselberth M B S, Aarts J and Lahabi K 2021 Direct-write printing of Josephson junctions in a scanning electron microscope *ACS Nano* **15** 322
[33] Linder J and Robinson J 2015 Superconducting spintronics *Nat. Phys.* **11** 307